

Article

Use of Remote Sensing to Assess the Water-Saving Effect of Winter Wheat Fallow

Liang Zhai ^{1,2} , Xianghui Gu ^{3,*}, Yajing Feng ^{1,2}, Dongqing Wu ^{4,5,6} and Tengbo Wang ^{1,2}

¹ Research Center for Natural Resources Surveying and Monitoring, Chinese Academy of Surveying and Mapping, Beijing 100036, China; zhailiang@casm.ac.cn (L.Z.); fengyajing1233@163.com (Y.F.); 202083020076@sdust.edu.cn (T.W.)

² Key Laboratory of Surveying and Mapping Science and Geospatial Information Technology of Ministry of Natural Resources, Beijing 100036, China

³ National Marine Data and Information Service, Tianjin 300171, China

⁴ Faculty of Geomatics, Lanzhou Jiaotong University, Lanzhou 730070, China; 11200871@stu.lzjtu.edu.com

⁵ National-Local Joint Engineering Research Center of Technologies and Applications for National Geographic State Monitoring, Lanzhou 730070, China

⁶ Gansu Provincial Engineering Laboratory for National Geographic State Monitoring, Lanzhou 730070, China

* Correspondence: xianghuigu@126.com

Abstract: Winter wheat fallow policy has a greater effect on water resource management, and the water-saving effect in the fallow process of winter wheat can provide data support for precise water resource utilization planning. In order to evaluate the water resource consumption of winter wheat and the related effect from winter wheat fallow, this study searched the changing trends of cultivated land evapotranspiration under five different scenarios through the object-oriented extraction method and a SEBS model based on multi-source data. The results indicated that the evapotranspiration during winter wheat growing period was higher than that of winter wheat fallow land, and there was no big difference in evapotranspiration between the fallow land during harvesting and the emergence of new crops. The evapotranspiration of winter wheat was higher than that of various fallow land, and the evapotranspiration of abandoned land was higher than other fallow land in the winter wheat growing season. From this point, this study concludes that the fallow land policy can effectively reduce evapotranspiration during the growing of winter wheat, which is conducive to the sustainable exploiting of water resources.

Keywords: water resource sustainable development; remote sensing; water-saving effect; evapotranspiration



Citation: Zhai, L.; Gu, X.; Feng, Y.; Wu, D.; Wang, T. Use of Remote Sensing to Assess the Water-Saving Effect of Winter Wheat Fallow. *Sustainability* **2021**, *13*, 10192. <https://doi.org/10.3390/su131810192>

Academic Editors: Agostina Chiavola and Giovanni De Feo

Received: 20 July 2021

Accepted: 7 September 2021

Published: 13 September 2021

Publisher's Note: MDPI stays neutral with regard to jurisdictional claims in published maps and institutional affiliations.



Copyright: © 2021 by the authors. Licensee MDPI, Basel, Switzerland. This article is an open access article distributed under the terms and conditions of the Creative Commons Attribution (CC BY) license (<https://creativecommons.org/licenses/by/4.0/>).

1. Introduction

Water resources are scarce in the North China Plain with insufficient precipitation and river water. In order to carry out agricultural production, a large amount of groundwater is extracted for irrigation, especially for the winter wheat growth during which the precipitation is low [1,2]. Long-term over-exploitation of groundwater has caused the levels of shallow groundwater to drop. The Pilot Implementation Plan of Cultivated Land Seasonal Fallow System in Hebei Province was issued by the Department of Agriculture and Rural Development of Hebei Province and the Department of Finance of Hebei Province, China on 2 July 2019 [3]. In this plan, both natural fallow and ecological fallow were recommended in order to obtain the benefits of seasonal fallow. Satellite remote sensing was proposed to be employed for the tracking and monitoring of seasonal fallow land. We could understand the changes in surface water through evapotranspiration, which helps to clarify the role of winter wheat fallow in water conservation and provide scientific data support for the sustainable development of water resources [4,5]. Therefore, it was desired to quantitatively describe the changes in surface water evapotranspiration during the fallow period of winter wheat.

Previously, a number of studies for fallow land information extraction and evapotranspiration calculation were proposed through crop classification and evapotranspiration models. There are many remote sensing crop classification methods such as time-series vegetation index [6], supervised classification [7], decision tree [8,9], and neural networks [10,11], where the time-series vegetation index method has a better classification effect but requires a higher temporal resolution. To meet higher temporal resolution, the existing time-series vegetation index usually used these combinations in previous studies: MODIS-EVI [12], MODIS-NDVI [13], Landsat-NDVI [14,15], MODIS-Multi-Index [16], and Multi-Source Satellite-NDVI [17]. Sentinel-2 has a relatively high spatial resolution (10 m for visible light and near infrared) and temporal resolution (10 days, five days after the launch of Sentinel-2b in 2017), and its temporal resolution was sufficient to capture the vegetation phenology information. Therefore, many scholars have carried out research based on Sentinel-2 time series data in vegetation classification [18–20], vegetation health status monitoring [21], yield estimation [22,23], etc. For example, Magnus Persson [18] used Sentinel-2 time-series data to classify tree species in central Sweden and compared the sensitivity of Sentinel-2 to the classification; Sébastien Rapinela [19] used time-series Sentinel-2 data to classify vegetation communities on the grassland, and proved that time series data were better than single date and single band data in the classification accuracy of vegetation types; Patrick Griffiths [20] used Sentinel-2 and Landsat combined time series data to realize the mapping of German crop types; moreover, Mariana Belgiu [24] used the time-weighted dynamic time warping algorithm (TWDTW) for object-based classification, and compared the pixel-based TWDTW algorithm with the random forest algorithm, and the object-based TWDTW algorithm with the random forest algorithm.

Most of the evapotranspiration models have been proposed based on radiative transfer theory such as SEBAL and SEBS. Penman [25] first proposed the concept of potential evapotranspiration and the calculation formula of evapotranspiration without horizontal water vapor transportation and then proposed a model to obtain the evapotranspiration on a single leaf based on the research of the water and transpiration mechanism. Menenti proposed the SEBI model, which used the relationship between surface temperature and evapotranspiration to realize the parameterization of evapotranspiration [26]. Bastiaanssen developed the SEBAL algorithm, which was based on the surface energy balance equation and added a method to calculate latent heat flux [27,28]. Su [29] proposed a SEBS model consistent with the basic principles of the SEBAL algorithm that no longer uses the remainder method to calculate the instantaneous evapotranspiration, but calculates the evaporation ratio by determining the latent heat flux of the dry and wet limit, and then calculates the daily evapotranspiration by the relatively constant evaporation ratio. Later, some scholars improved the calculation method of daily evapotranspiration and the method of obtaining parameters on the basis of the SEBS model [30].

In past research, the research on fallow land has mainly focused on social, economic, and extraction methods [31], while few studies have on the water-saving effect with irrigation [32,33]. Research on evapotranspiration calculation with SEBS mostly uses MODIS data, which have low spatial resolution for large-area, and Landsat data [34], which has low temporal resolution for a single day. The research of fallow land and evapotranspiration has been relatively independent, while few have been conducted on the evapotranspiration of fallow land, and it is difficult to balance the high temporal resolution and high spatial resolution that is needed in the water-saving research of winter wheat fallow.

Therefore, as an extension of previous studies, the aim of this study was to obtain multi-temporal, high-resolution evapotranspiration distribution trends and accurate evapotranspiration data of winter wheat and fallow land by breaking through the limitations of existing remote sensing platforms, implementing multi-source data collaboration methods and exploring multi-source remote sensing data evapotranspiration inversion research programs. We chose Hengshui City, Hebei Province as the research area in the study as it is located in the North China Plain where there is much winter wheat fallow land.

2. Data and Methods

In order to explore the evapotranspiration changes between the fallow land and planting areas of winter wheat, a general analysis framework was proposed as follows: First, according to the phenological characteristics of winter wheat and fallow land, winter wheat and fallow land were extracted from the remote sensing images. Then, the surface energy balance system (SEBS), a relatively perfect evapotranspiration inversion method, was used to retrieve the evapotranspiration. Finally, the evapotranspiration trend of winter wheat and fallow land was obtained to analyze the impact of winter wheat fallow on the sustainable use of water resources.

2.1. Multi-Source Data Processing

The data mainly include the remote sensing data that were used to calculate the surface parameters (e.g., Sentinel-2 data and Landsat 8 data), and the meteorological data that were used for analyzing atmospheric parameters such as temperature and pressure, and surface temperature products.

Remote sensing data includes Sentinel-2 data, Landsat 8 data, and MODIS data. Sentinel-2 is a European wide-swath, high-resolution, multi-spectral imaging mission. The full mission specification of the twin satellites flying in the same orbit but phased at 180°, is designed to give a high revisit frequency of five days at the Equator. Sentinel-2 carries an optical instrument payload that samples 13 spectral bands: four bands at 10 m, six bands at 20 m, and three bands at 60 m spatial resolution. Sentinel-2 data can be downloaded from the European Space Agency (ESA) (<https://scihub.copernicus.eu/dhus/#/home>, accessed on 18 July 2021). The Landsat 8 satellite payload consists of two science instruments—the Operational Land Imager (OLI) and the Thermal Infrared Sensor (TIRS). These two sensors provide seasonal coverage of the global landmass at a spatial resolution of 30 m (visible, NIR, SWIR); 100 m (thermal); and 15 m (panchromatic). A Landsat 8 scene size is 185 km × 180 km and can be downloaded from the U.S. Geological Survey (USGS) (<https://glovis.usgs.gov/>, accessed on 18 July 2021). The MODIS has a viewing swath width of 2330 km and views the entire surface of the Earth every one to two days. Its detectors measure 36 spectral bands between 0.405 and 14.385 μm, and it acquires data at three spatial resolutions—250 m, 500 m, and 1000 m. MODIS data can be downloaded from the National Aeronautics and Space Administration (NASA) (<https://ladsweb.modaps.eosdis.nasa.gov/>, accessed on 18 July 2021).

Due to the lack of thermal infrared bands in Sentinel data, the surface temperature cannot be retrieved. Landsat 8 and MODIS surface temperature products are used to supplement Sentinel data. Sentinel-2 data and Landsat 8 data require radiometric calibration and atmospheric correction to generate apparent reflectance and emissivity, and MODIS temperature products need to be reprocessed.

Meteorological data came from daily station observations from the China Meteorological Data Network including air pressure, temperature, relative humidity, wind direction and speed, precipitation, evaporation, sunshine, and ground temperature. In order to avoid the errors in the marginal area, the sites around the study area were processed together when selecting sites. Next, we performed normalized conversion, format conversion, and quantitative relationship conversion on the data to obtain daily raster data of air pressure, relative humidity, wind speed, and sunshine.

In addition, the wind speed was observed at 10 m, while other meteorological elements were measured at 2 m. Therefore, the wind speed at 10 m was converted to the wind speed at 2 m for the SEBS model applications. The conversion formula can be expressed as follows [35]:

$$U_2 = U_{10} \frac{4.87}{67.8 * 10 - 5.42} \quad (1)$$

where U_2 and U_{10} are the wind speed at 2 m and 10 m, respectively.

The specific humidity in the SEBS model can be calculated from relative humidity, temperature, and air pressure:

$$q = \frac{0.622 * e_s * K}{(P - 0.378e_s) * 100} \quad (2)$$

where K and P are the relative humidity and the air pressure, respectively.

e_s is the saturated vapor pressure, which can be expressed from temperature t :

$$e_s = 6.1078e^{\frac{17.27(t-273.16)}{t-35.86}} \quad (3)$$

2.2. Object-Oriented Extraction Method

The extraction of winter wheat and fallow land was based on the phenology and growth cycle length. Phenological information refers to the vegetation index and other indicators for reflecting vegetation state from crops sowing to harvest. Crops with different growth cycles have various change trends for the related indicators under the same time. The phenological information on the remote sensing data is reflected as the image changes over time. The long-term series data with a stronger anti-noise ability can effectively represent vegetation phenological information [17,36].

The normalized difference vegetation index (NDVI) is the significant indicators for reflecting the response characteristics of vegetation reflectance increase in the near-infrared band. NDVI that is affected by pigment and structure can effectively reflect the regular changes under different growth stages of crops. Due to different crops with special NDVI during the whole growth period, the vegetation index combined with time-series information can explore growth period and growth state to distinguish the crops.

The multi-resolution segmentation algorithm (MRS) was applied for image segmentation through aggregating pixels into objects by iterating from the pixel level (Trimble, 2011). Datasets of various extents were generated by partitioning each image into regular tiles. The smallest tile size was 100×100 pixels, which doubled iteratively, until there was no further partition, and the image was processed at its full extent. The geometric accuracy improvement in quality rate during the multi-resolution segmentation was performed in smaller extents compared to the whole image segmentation [37].

MRS algorithms were provided by the eCognition[®] software (Trimble, 2011), which requires image layer weight, scale parameter, shape factor, and compactness factor. The scale parameter determines the degree of segmentation. More object units are segmented as smaller scale parameters with a smaller single area. In order to avoid trial and error and the uncertainty of subjective selection, the Estimation of Scale Parameters 2 (ESP2) [38] was used to assist, which relies on the cross-scale local variance to automatically identify three suitable scale parameters for hierarchical segmentation.

The curve matching method as an effective method for long-term data classification was integrated with the system analysis framework. The curve changes caused by phenological shift for crop classification were limited to advance or delay (translation) due to the growth period compression or extension (tension). The curve had a small change range, and similar crops had closer time-series NDVI curves.

The time-series NDVI curve was calculated for each object after segmentation. Through matching the calculated time-series NDVI curve with the reference time-series vegetation index curve, the crops can be classified according to the matching results. The matching algorithm was time-weighted dynamic time warping. The algorithm uses a twist function to describe the time correspondence between the curve to be matched and the reference curve. The classification criteria can efficiently discriminate fallowed and non-fallowed objects, as shown in Table 1.

Table 1. Land use classification system and description.

Land Use Classification	Winter Wheat Fallow Type	Description
Winter wheat	–	Arable land with winter wheat
Winter wheat fallow	Spring corn	Arable land without winter wheat but with spring corn
	Summer corn	Arable land without winter wheat but with summer corn
	Abandoned	Arable land without crop
Town	–	City and the artificial facilities such as building, road
Water	–	Water
Other vegetation	–	Features with vegetation characteristics but not belong to above

2.3. Inversion of Surface Evapotranspiration

The evapotranspiration inversion was based on SEBS, which consists of a set of tools for the determination of the land surface physical parameters such as albedo, emissivity, temperature, vegetation coverage, etc. from spectral reflectance and radiance measurements; a model for the determination of the roughness length for heat transfer; and a new formulation for the determination of the evaporative fraction on the basis of energy balance at limiting cases [29]. The inversion principle of the SEBS model is based on the energy balance between the energy received on the Earth's surface and that used for surface and soil temperature increase, water evaporation, and biological photosynthesis. According to the energy balance principle, the energy relationship on the surface can be expressed as:

$$R = G + H + \lambda E + PH \quad (4)$$

where R is the net radiation that denotes the energy of net surface absorbed or consumed; G is the soil heat flux for the heat exchanged between the soil surface layer and vegetation; H is the turbulent sensible heat flux; λE is the turbulent latent heat flux, where λ is the latent heat of vaporization of water; and E is the evapotranspiration. PH is the biomass energy increased by vegetation photosynthesis with a small and negligible value.

According to the SEBS, R requires surface albedo, emissivity, and land surface temperature, G requires vegetation coverage, and H requires meteorological data. The emissivity and vegetation coverage are easy to obtain, while the surface albedo needs to be reflected by different parameters. The Sentinel-2 data do not have thermal infrared bands and cannot directly retrieve the temperature. The land surface temperature is replaced by the predicted Landsat 8 temperature, which was fused by MODIS temperature sequence and Landsat 8 surface temperature. Since the estimated temperature is asynchronous with Sentinel-2, we compared the results of the Sentinel-2 inversion with the results of Landsat 8 during the following experiment to ensure that the results were available.

The fusion method in this study was the spatio-temporal integrated temperature fusion model (STITFM), which is based on the assumption that the difference of the same homogeneous surface is uniform on different sensors. Assuming that the land-cover type and sensor calibration does not change between dates T_1 , T_2 , and T_3 , then the residual would also not change from dates T_1 , T_2 , and T_3 . Furthermore, random noise is neglected [39]. The difference between the MODIS sensor and the Landsat sensor at the same time is regarded as the error between the two sensors, and the error in T_2 can be calculated through T_1 and T_3 (Figure 1).

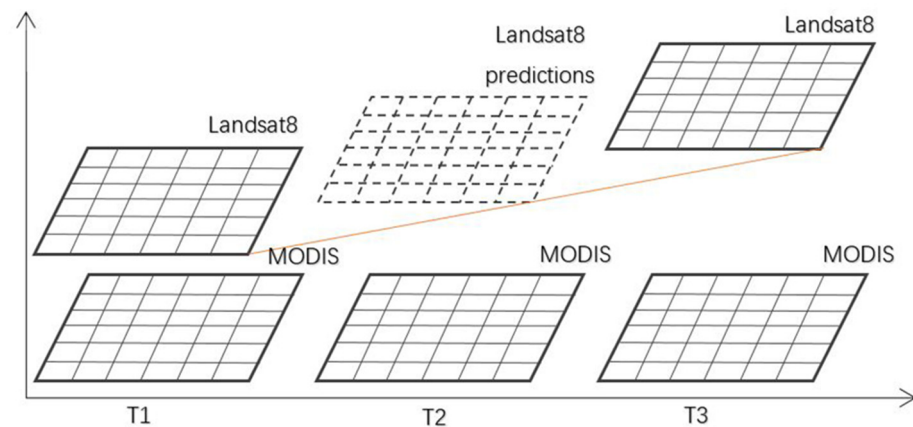


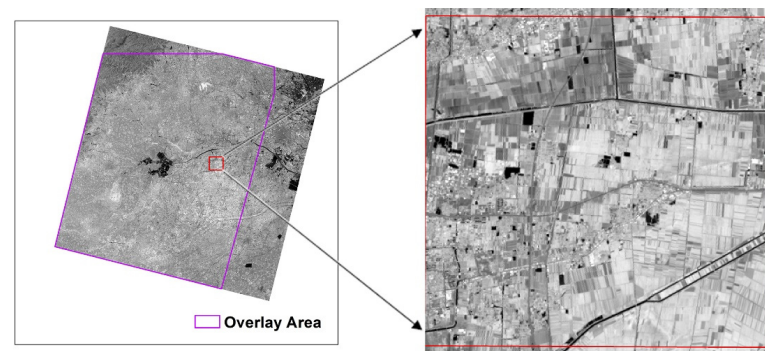
Figure 1. The sketch map of the surface temperature fusion principle.

Direct surface albedo is the main factor that affects the radiated energy of the ground. The single-band reflectance of Sentinel-2 multi-spectral data needs to be converted to wide-band albedo, and the conversion formula is as follows [40]:

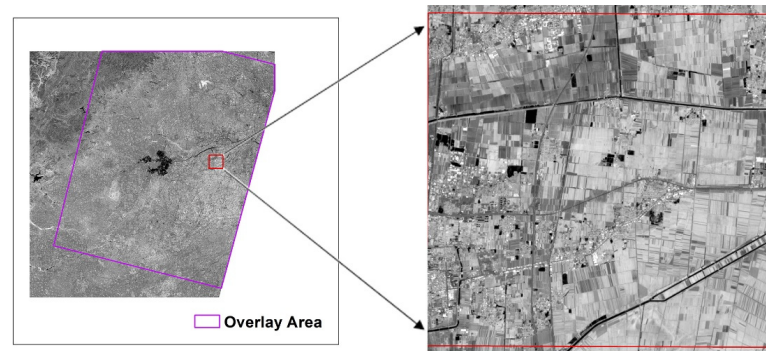
$$\alpha = 0.2688\alpha_2 + 0.0362\alpha_3 + 0.1501\alpha_4 + 0.3045\alpha_{8A} + 0.1644\alpha_{11} + 0.0356\alpha_{12} - 0.0049 \quad (5)$$

where α_i is the reflectance of the i band.

In order to verify the accuracy of the surface reflectance results, the area that Landsat 8 and Sentinel-2 passed at the same time on 13 May 2019 were selected. As shown in Figure 2, the results of Landsat 8 and Sentinel-2 data were consistent with the approximate texture and brightness. The surface albedo of Sentinel-2 was sharper than that of Landsat 8 with high contrast and distinct boundaries.



(a) Landsat 8 inversion results and partial enlarged view



(b) Sentinel-2 inversion results and partial enlarged view

Figure 2. The comparison of surface reflectance between Sentinel-2 and Landsat 8.

2.4. Analysis on Sustainable Utilization of Fallow Water Resources

The spatial overlay analysis and region analysis were used to process the winter wheat fallow and inversion evapotranspiration, and the comparative analysis was conducted on winter wheat and winter wheat fallow that contained spring corn, summer corn, and abandoned land. The obtained analysis for the evapotranspiration difference between the fallow land and winter wheat planting areas was used for comparing the related water resource consumption and water saving effects.

3. Process and Discussion

3.1. Fallow Extraction

An object-oriented time-series vegetation index curve matching method was applied for the extraction of winter wheat and fallow. Based on the whole growing season of winter wheat, the time-series index curve was constructed from January 2019 to October 2019. More than ten winter wheat plots were uniformly selected as samples, and the vegetation index of samples at each time point was calculated to construct the reference time-series vegetation index. NDVI average values of each time-series for each object were calculated for the segmented time series vegetation index image, and the time-series vegetation index curves were proposed to match with the reference time-series vegetation index curve to be classified (Figure 3).

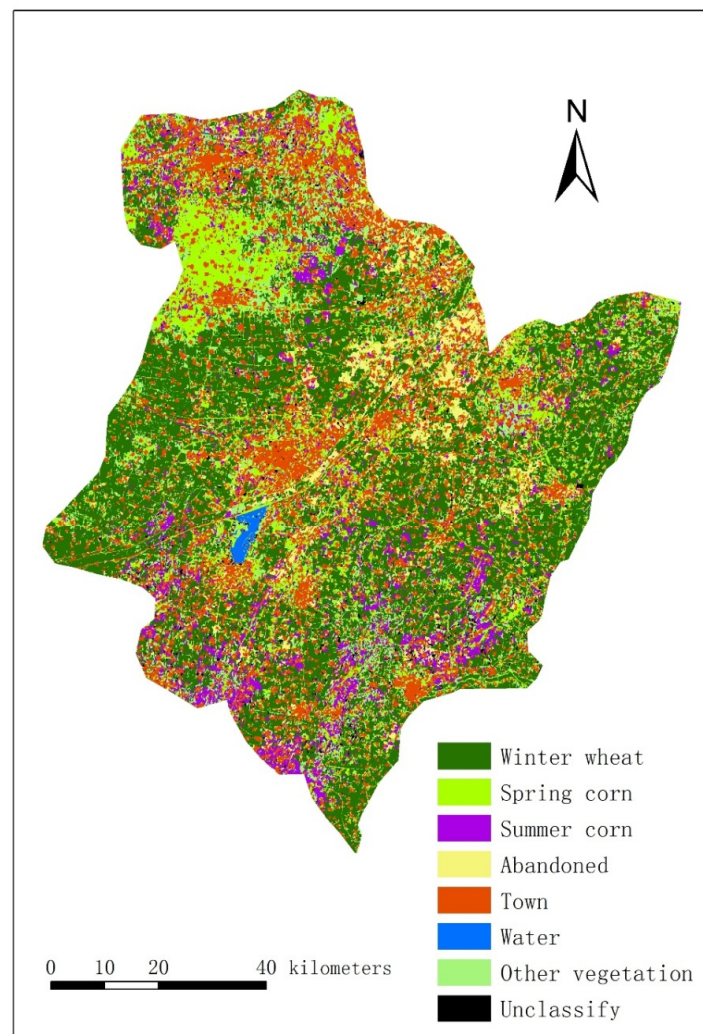


Figure 3. Land use classification map of Hengshui.

3.2. Evapotranspiration Inversion

According to the principle of the SEBS model, evapotranspiration is derived from surface net radiant fluxes, soil heat flux, and sensible heat flux. The evaporation ratio can be calculated under two extreme conditions of “extremely dry” and “extremely wet” to analyze the daily evapotranspiration. Comparing the remote sensing inversion results of the SEBS model with the reference crop evapotranspiration based on the PM formula, it was found that the results from the SEBS model were in a greater agreement with the PM model. Root mean square errors were 0.5366 on 13 May and 0.5433 on 23 May.

Compared with the Sentinel-2 data, Landsat 8 data have theoretical advantages in calculating single-day evapotranspiration and can directly obtain the surface temperature of the corresponding time of the image. However, Landsat 8 does not have advantages in revisit period resolution, so Landsat 8 data are used as a time sequence supplement and a source of surface temperature images. At the same time, in order to explore the impact of indirect surface temperature on the inversion of evapotranspiration through Sentinel-2 data, a comparative experiment was conducted to study the effects of asynchronous parameters. The result showed a very small difference between the results of Sentinel-2 and Landsat 8.

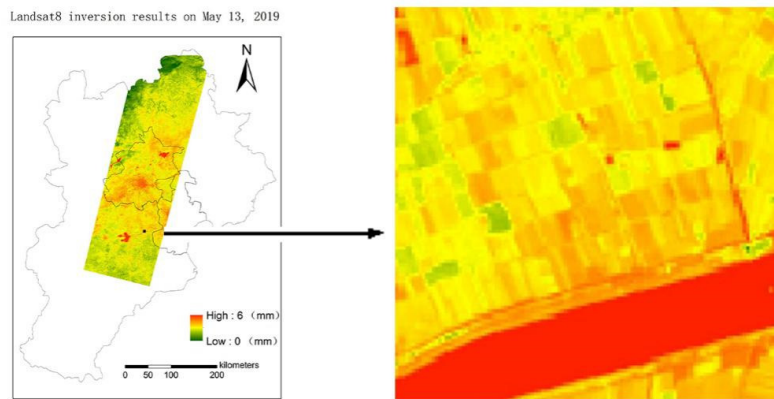
The area that Landsat 8 and Sentinel-2 passed at the same time on 13 May was selected, and the Landsat 8 and Sentinel-2 data were separately used to invert surface parameters including surface emissivity and albedo. Common meteorological parameters and surface parameters were used to retrieve evapotranspiration.

In general, the evapotranspiration retrieved by Sentinel-2 and Landsat 8 on 13 May were completely consistent in spatial distribution. High evapotranspiration areas all appeared in Beijing’s main town area and lakes, and the low evapotranspiration areas all appeared at the northwest border, and the overall distribution was completely consistent, as shown in Figure 4. There were 91% and 91.8% of the results from Sentinel-2 and Landsat 8 with a distributed interval value of [3, 4.2], respectively.

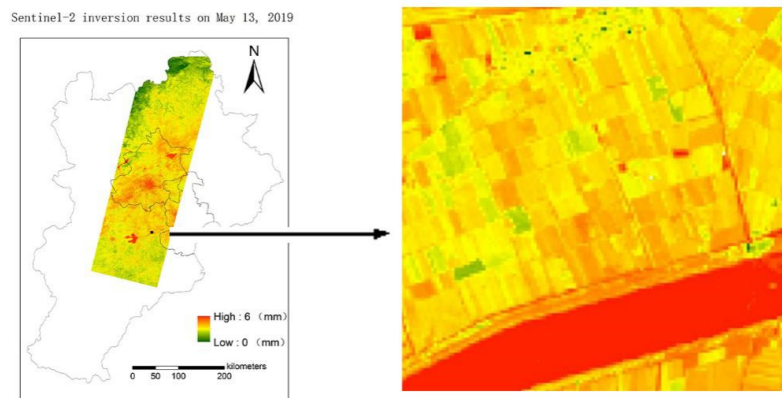
In addition, 89,172-pixel pairs in the range were uniformly selected to further explore the relationship between the results from Sentinel-2 and Landsat 8 inversion. The results show that the root mean square error between Sentinel-2 and Landsat 8 inversion was 0.1193. The linear regression result R^2 was 0.8934, and the linear regression coefficient was 0.9575 (Figure 5).

Through the comparison between the Sentinel-2 inversion results and Landsat 8 inversion results, the evapotranspiration from Sentinel-2 inversion is feasible. The results from Sentinel-2 and Landsat 8 inversion were highly consistent in numerical distribution and spatial distribution. There were some outliers in the low-value area. A total of 45 outliers were deviated more than 1 mm, which was negligible compared to the total number of samples of 89,172.

In order to specifically analyze the change law of evapotranspiration of winter wheat and fallow land, the superposition analysis of daily evapotranspiration and the range of fallow land was carried out to obtain the variation curve of evapotranspiration of winter wheat and fallow land over time to explore the change trend in evapotranspiration.



(a) Landsat 8 inversion evapotranspiration and partial enlarged view



(b) Sentinel-2 inversion evapotranspiration and partial enlarged view

Figure 4. The comparison of Sentinel-2 and Landsat8 inversion evapotranspiration.

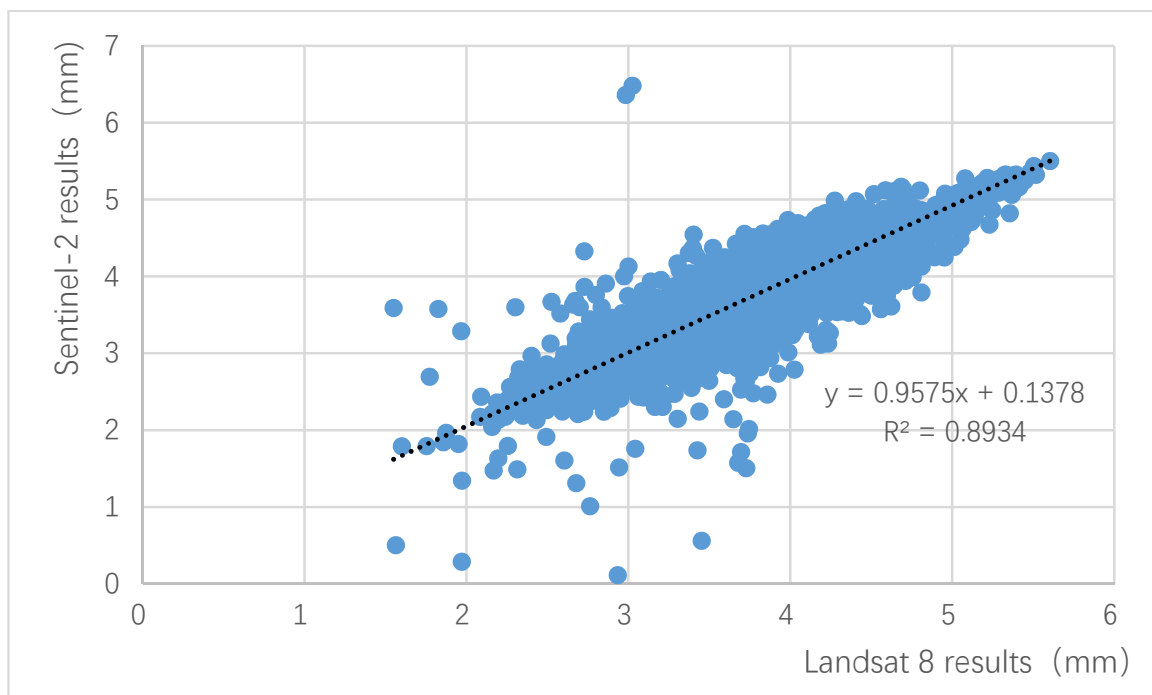


Figure 5. Scatter plot of inversion results of Sentinel-2 and Landsat 8.

3.3. Effect of Winter Wheat Fallow Land on Evapotranspiration

The evapotranspiration of winter wheat and fallow land during the remote sensing monitoring dates showed an increasing trend with the passage of time, but some of the days indicated a slight decrease. In addition, winter wheat and fallow land had similar trends. When the evapotranspiration of winter wheat decreased, the evapotranspiration of fallow land presented a corresponding decrease. Similar trends were related to the meteorological and atmospheric conditions on that day.

We compared the evapotranspiration under five scenarios in Table 2. The total evapotranspiration of winter wheat during the remote sensing monitoring dates was 117.69 mm, and the evapotranspiration before the harvest date (June 9) was 62.01 mm. In fallow land, the evapotranspiration of spring corn, summer corn, and abandoned farmland were 57.50 mm, 56.67 mm, and 57.97 mm, respectively, while as a reference, the town evapotranspiration was 58.22 mm. The evapotranspiration of fallow winter wheat was reduced by about 8%.

Table 2. Statistics of evapotranspiration in Hengshui.

Date Range	Town	Spring Corn	Winter Wheat	Summer Corn	Abandoned
3 January 2019–9 June 2019 ¹	58.22	57.50	62.01	56.67	57.97
9 June 2019–27 July 2019	56.99	58.50	55.68	55.93	54.92
3 January 2019–27 July 2019	115.21	115.85	117.69	112.60	112.89

¹ 9 June 2019 was the day closest to the harvest date in Hengshui.

The evapotranspiration of summer corn in fallow land was lower than that in winter wheat planting areas from January to May. Compared with winter wheat, the evapotranspiration of summer corn was similar in January, and slightly higher in May. From mid-April to mid-June, the evapotranspiration of winter wheat was significantly higher than that of summer corn in fallow land. Winter wheat grew vigorously, and the evapotranspiration increased obviously during the period (Figure 6).

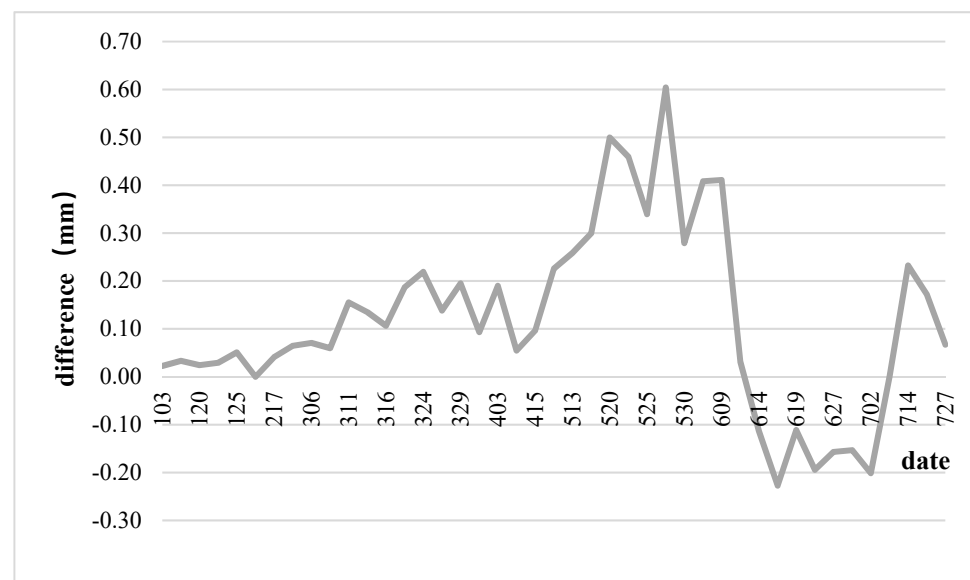


Figure 6. Difference in evapotranspiration between winter wheat and summer corn.

Moreover, the summer corn area was in a fallow state for planting during this period, and the surface evapotranspiration was small. After June 9, winter wheat began to mature and harvest, and the evapotranspiration was substantially reduced.

In contrast, the difference in evapotranspiration between winter wheat and spring corn in fallow land was relatively small. An abnormal point appeared in mid-March. On

that date, the image was incomplete and the spring corn area was small, which led to sharp fluctuations in the difference. The fluctuations in mid-April were normal fluctuations that were caused by the difference in evapotranspiration growth rates between winter wheat and spring corn. During this period, winter wheat grew vigorously and evapotranspiration rose, and the evapotranspiration of spring corn had not increased yet. Then, spring corn entered the rapid growth period, the evapotranspiration gap narrowed, and the time span was large, resulting in a sharp decline in the image. The evapotranspiration trend in winter wheat after mid-June was consistent with that of summer corn (Figure 7).

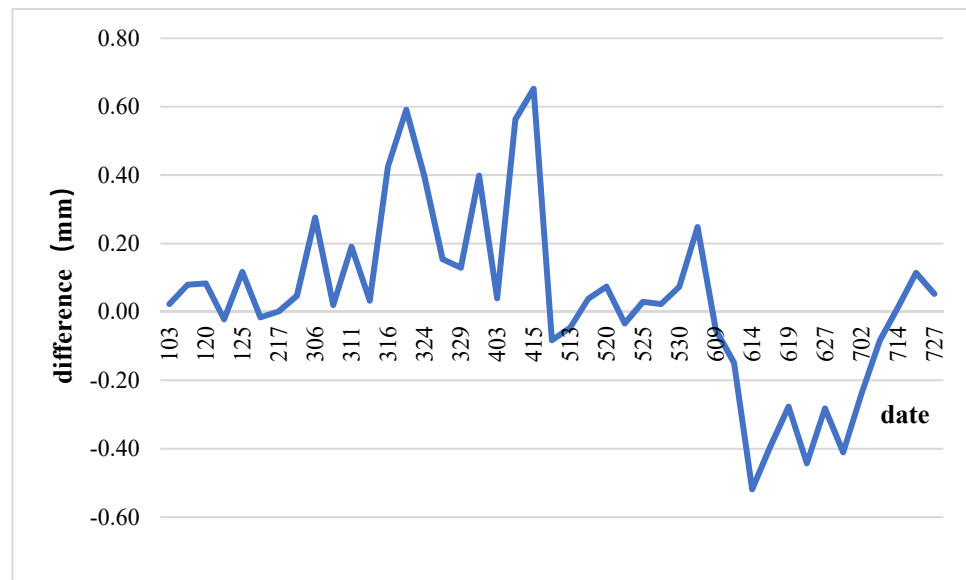


Figure 7. Difference in evapotranspiration between winter wheat and spring corn.

4. Conclusions

In this study, the time-series vegetation index method and the multi-source data SEBS model based on Sentinel-2 and Landsat 8 data were applied to analyze the impact of fallow land on the sustainable use of water resources systematically. The study indicates that the time-series vegetation index method can extract fallow land and its type effectively and provide a basis for the detailed study of evapotranspiration; the multi-source data from the SEBS model can provide multi-temporal, high-resolution evapotranspiration of fallow land and its change trends, which offer data support for policy formulation and affects the evaluation of the sustainable development of water resources.

The period when the dramatic evapotranspiration difference exhibited between winter wheat and fallow land was from mid-April to pre-harvest time. Winter wheat evapotranspiration was high during this period, and the evapotranspiration of winter wheat was not very different from fallow land between winter wheat harvest and the emergence of new crops during the period from the harvest of winter wheat to the emergence of new crops. In winter wheat fallow land, the evapotranspiration of cultivated land without crops during the winter wheat growing season was the lowest, but the evapotranspiration of abandoned land was higher than that of cultivated land with crops during the period from the harvest of winter wheat to the emergence of new crops.

Author Contributions: Methodology, L.Z. and X.G.; Data collection, processing and analysis, X.G.; Writing—original draft, X.G., Y.F. and D.W.; Writing—review and editing, L.Z., T.W. and X.G. All authors have read and agreed to the published version of the manuscript.

Funding: This research was funded by the Project for High-Level-Innovation Talents in Science and Technology, Ministry of Natural Resources, grant number: 1211060000018003908; the research projects of the Chinese Academy of Surveying and Mapping, grant number: AR2112.

Conflicts of Interest: The authors declare no conflict of interest.

References

- Li, J.; Inanaga, S.; Li, Z.; Eneji, A.E. Optimizing irrigation scheduling for winter wheat in the North China Plain. *Agric. Water Manag.* **2005**, *76*, 8–23. [CrossRef]
- Sun, H.; Shen, Y.; Yu, Q.; Flerchinger, G.N.; Zhang, Y.; Liu, C.; Zhang, X. Effect of precipitation change on water balance and WUE of the winter wheat–summer corn rotation in the North China Plain. *Agric. Water Manag.* **2009**, *97*, 1139–1145. [CrossRef]
- Notice on Implementation Plan of Seasonal Fallow System for Farmland Pilot in Hebei Province in 2019 Issued by Department of Agriculture and Rural Affairs of Hebei Province and Hebei Provincial Department of Finance. Available online: <http://nync.hebei.gov.cn/article/tzgg/201908/20190800014295.shtml> (accessed on 8 August 2021).
- Xu, Y.; Mo, X.; Cai, Y.; Li, X. Analysis on groundwater table drawdown by land use and the quest for sustainable water use in the Hebei Plain in China. *Agric. Water Manag.* **2005**, *75*, 38–53. [CrossRef]
- Shen, Y.; Zhang, Y.; Scanlon, B.R.; Lei, H.; Yang, D.; Yang, F. Energy/water budgets and productivity of the typical croplands irrigated with groundwater and surface water in the North China Plain. *Agric. For. Meteorol.* **2013**, *181*, 133–142. [CrossRef]
- Gao, Y.; Liu, Q.; Li, I.; Le, Y. A new method for multi-cropping cultivated land extraction based on temporal identification of time-series vegetation index characteristics. *Remote Sens. Technol. Appl.* **2015**, *30*, 431–438.
- Islam, A.; EL-Magd, T. Improvements in land use mapping for irrigated agriculture from satellite sensor data using a multi-stage maximum likelihood classification. *Int. J. Remote Sens.* **2003**, *24*, 4197–4206.
- Wang, L.; Guo, Y.; He, I.; Wang, L.; Zhang, X.; Liu, T. Sentinel-2A image crop extraction method based on decision tree and SVM. *Trans. Chin. Soc. Agric. Mach.* **2018**, *49*, 146–153.
- Du, B.; Zhang, I.; Wang, Z.; Mao, D.; Zhang, M.; Wu, B. Crop classification using Sentinel-2A NDVI time-series and object-oriented decision tree method. *J. Geo-Inf. Sci.* **2019**, *21*, 740–751.
- Yu, F.; Zhuo, Y.; Bao, Y. Land cover classification based on BP neural network and MODIS-EVI time-series. *Sci. Surv. Mapp.* **2008**, *33*, 203–204.
- Salas, E.A.L.; Subburayalu, S.K.; Slater, B.; Zhao, K.; Bhattacharya, B.; Tripathy, R.; Das, A.; Nigam, R.; Dave, R.; Parekh, P. Mapping crop types in fragmented arable landscapes using AVIRIS-NG imagery and limited field data. *Int. J. Image Data Fusion* **2019**, *11*, 33–56. [CrossRef]
- Zhang, I.; Feng, L.; Yao, F. Improved maize cultivated area estimation over a large scale combining MODIS–EVI time series data and crop Phenological information. *Isprs J. Photogramm. Remote Sens.* **2014**, *94*, 102–113. [CrossRef]
- Guo, Y.; Liu, Q.; Liu, G.; Huang, C. Research on the extraction of main crop planting information based on MODIS time-series NDVI. *J. Nat. Resour.* **2017**, *32*, 1808–1818.
- Yan, L.; Roy, D.P. Conterminous United States crop field size quantification from multi-temporal Landsat data. *Remote Sens. Environ.* **2016**, *172*, 67–86. [CrossRef]
- Roy, D.P.; Yan, L. Robust Landsat-based crop time series modelling. *Remote Sens. Environ.* **2020**, *238*, 110810. [CrossRef]
- Ping, Y.; Zang, S. Crop Identification Based on MODIS NDVI Time-series Data and Phenological Characteristics. *J. Nat. Resour.* **2016**, *31*, 503–513.
- Tian, H.; Huang, N.; Niu, Z. Mapping Winter Crops in China with Multi-Source Satellite Imagery and Phenology-Based Algorithm. *Remote Sens.* **2019**, *11*, 820. [CrossRef]
- Persson, M.; Lindberg, E.; Reese, H. Tree Species Classification with Multi-Temporal Sentinel-2 Data. *Remote Sens.* **2018**, *10*, 1794. [CrossRef]
- Rapinel, S.; Mony, C.; Lecoq, L.; Clément, B.; Thomas, A.; Hubert-Moy, L. Evaluation of Sentinel-2 time-series for mapping floodplain grassland plant communities. *Remote Sens. Environ.* **2019**, *223*, 115–129. [CrossRef]
- Griffiths, P.; Nendel, C.; Hostert, P. Intra-annual reflectance composites from Sentinel-2 and Landsat for national-scale crop and land cover mapping. *Remote Sens. Environ.* **2019**, *220*, 135–151. [CrossRef]
- Zarco-Tejada, P.; Hornero, A.; Hernández-Clemente, R.; Beck, P.S.A. Understanding the temporal dimension of the red-edge spectral region for forest decline detection using high-resolution hyperspectral and Sentinel-2a imagery. *Isprs J. Photogramm. Remote Sens.* **2018**, *137*, 134–148. [CrossRef]
- Lambert, M.; Traoré, P.C.S.; Blaes, X.; Baret, P.; Defourny, P. Estimating smallholder crops production at village level from Sentinel-2 time series in Mali’s cotton belt. *Remote Sens. Environ.* **2018**, *216*, 647–657. [CrossRef]
- Kolecka, N.; Ginzler, C.; Pazur, R. Regional Scale Mapping of Grassland Mowing Frequency with Sentinel-2 Time Series. *Remote Sens.* **2018**, *10*, 1221. [CrossRef]
- Belgiu, M.; Csillik, O. Sentinel-2 cropland mapping using pixel-based and object-based time-weighted dynamic time warping analysis. *Remote Sens. Environ. Interdiscip. J.* **2018**, *204*, 509–523. [CrossRef]
- Penman, H.L. Natural evaporation from open water, bare soil and grass, Proceedings of the Royal Society of London A: Mathematical. *Phys. Eng. Sci. (The Royal Society)* **1948**, *193*, 120–145.
- Menenti, M. Understanding land surface evapotranspiration with satellite multispectral measurements. *Adv. Space Res.* **1993**, *13*, 89–100. [CrossRef]
- Bastiaanssen, W.G.M.; Menenti, M.; Feddes, R.A.; Holtslag, A.A.M. A remote sensing surface energy balance algorithm for land (SEBAL). 1. Formulation. *J. Hydrol.* **1998**, *212*, 198–212. [CrossRef]

28. Bastiaanssen, W.G.; Pelgrum, H.; Wang, J.; Ma, Y.; Moreno, J.F.; Roerink, G.J.; Van der Wal, T. A remote sensing surface energy balance algorithm for land (SEBAL) 2: Validation. *J. Hydrol.* **1998**, *212*, 213–229. [[CrossRef](#)]
29. Su, Z. The Surface Energy Balance System (SEBS) for estimation of turbulent heat fluxes. *Hydrol. Earth Syst. Sci.* **1999**, *6*, 85–100. [[CrossRef](#)]
30. Wu, Y.; Tian, G.; Wang, Y. Research on crop water requirement based on improved SEBS model. *Agric. Res. Arid Areas* **2015**, *33*, 113–118.
31. Xie, H.; Cheng, L.; Lu, H. Farmers' responses to the winter wheat fallow policy in the groundwater funnel area of China. *Land Use Policy* **2018**, *73*, 195–204. [[CrossRef](#)]
32. Wang, P. Investigation of seasonal fallow in Guantao County. *Mod. Rural Sci. Technol.* **2016**, *13*, 37–38.
33. Li, X. Investigation and analysis of water-saving effect in ingxian County's 2018 seasonal fallow pilot area. *Grassroots Agric. Technol. Ext.* **2019**, *7*, 43–45.
34. Li, Q. Research on Estimation of Surface Evapotranspiration Based on SEBS Model. Master's Thesis, North China University of Water Resources and Electric Power, Zhengzhou, China, 2019.
35. Hao, I. Study on Evapotranspiration Based on SEBS model in Handan. Master's Thesis, Hebei University of Engineering, Handan, China, 2018.
36. Wang, X.; Yin, S.; Liu, D.; Li, H.; Karim, S. Accurate playground localisation based on multi-feature extraction and cascade classifier in optical remote sensing images. *Int. J. Image Data Fusion* **2020**, *11*, 233–250. [[CrossRef](#)]
37. Drăguț, L.; Belgiu, M.; Popescu, G.; Bandura, P. Sensitivity of multiresolution segmentation to spatial extent. *Int. J. Appl. Earth Obs. Geoinf.* **2019**, *81*, 146–153. [[CrossRef](#)]
38. Drăguț, L.; Csillik, O.; Eisank, C.; Tiede, D. Automated parameterisation for multi-scale image segmentation on multiple layers. *ISPRS Photogramm. Remote Sens.* **2014**, *88*, 119–127. [[CrossRef](#)] [[PubMed](#)]
39. Wu, P.; Shen, H.; Zhang, L. Integrated fusion of multi-scale polar-orbiting and geostationary satellite observations for the mapping of high spatial and temporal resolution land surface temperature. *Remote Sens. Environ.* **2015**, *156*, 169–181. [[CrossRef](#)]
40. Li, Z.; Erb, A.; Sun, Q.; Liu, Y.; Shuai, Y.; Wang, Z.; Boucher, P.; Schaaf, C. Preliminary assessment of 20-m surface albedo retrievals from sentinel-2A surface reflectance and MODIS/VIIRS surface anisotropy measures. *Remote Sens. Environ.* **2018**, *217*, 352–365. [[CrossRef](#)]